Polybenzimidazole-membrane-based PEM fuel cell in the temperature range of 120–200 °C

Jianlu Zhang, Yanghua Tang, Chaojie Song, Jiujun Zhang *

Institute for Fuel Cell Innovation, National Research Council of Canada, Vancouver, BC V6T 1W5, Canada

Abstract

Phosphoric acid-doped polybenzimidazole-membrane-based PEM fuel cells were tested in the temperature range of 120–200 °C, with ambient backpressure and 0% RH. AC impedance spectroscopy, surface cyclic voltammetry and fuel cell performance simulation were used to obtain the exchange current densities for the cathodic oxygen reduction reaction (ORR) and anodic hydrogen oxidation reaction (HOR) on platinum-based catalysts at such high temperatures. The activation energies for ORR, HOR and membrane conductivity were also obtained separately. The results showed that temperature significantly affects the charger transfer and gas (O_2 and H_2) diffusion resistances. The effect of O_2 stoichiometry (ST_{air}) on fuel cell performance was also investigated. Increasing ST_{air} can effectively increase the O_2 partial pressure in the feed air, leading to improvements in both the thermodynamics and the kinetics of the fuel cell reactions. In addition, it was observed that increasing ST_{air} could also improve the gas diffusion processes.
© 2007 Elsevier B.V. All rights reserved.

Keywords: Phosphoric acid-doped polybenzimidazole (PBI); High-temperature PEM fuel cells; AC impedance spectroscopy (EIS); Oxygen reduction; Hydrogen oxidation; Exchange current density

1. Introduction

High-temperature (90–200 °C) proton exchange membrane fuel cells (PEMFCs) have been considered the next generation of fuel cell because of their advantages over those operated at lower temperatures (usually below 80 °C). These advantages include: (1) faster electrochemical kinetics, (2) improved and simplified water management, (3) effective thermal management and (4) improved contamination tolerance [1,2].

However, several challenges posed by high-temperature operation have been identified in recent years. The largest challenge is proton exchange membrane (PEM) materials. Perfluorosulfonic acid (PFSA) membranes (such as Nafion) are the most widely used for conventional PEM fuel cells operated at temperatures below 90 °C. Theoretically, Nafion-based membranes can be operated at temperatures lower than the glass transition value of ~130 °C [3,4]. However, in the range of 90–130 °C, the structural and chemical degradation of the membrane material

is faster [5,6]. In addition, because the conductivity of PFSA membranes depends on the water content, these membranes become dehydrated at higher operating temperatures, resulting in decreased proton conductivity. The decrease in conductivity thus leads to a decrease in fuel cell performance.

In addressing this issue, tremendous effort has focused on the development of and fabrication methods for high-temperature membranes [7]. In recent years, a polybenzimidazole (PBI) membrane, with a reported glass transition temperature of 420 °C [8] has been shown promise for high-temperature operation due to its high thermal stability [9]. Although the proton conductivity of pure PBI is very low, after it has been doped by some acids [10] remarkable high proton conductivity can be achieved even in an anhydrous state, due to its special proton conduction mechanism [11,12]. The most frequently used dopant is phosphoric acid, introduced in 1995 by Wainright et al. [13] for fuel cell applications. Since then, significant improvements have been made in membrane conductivity and fuel cell performance. The results obtained have shown that PBI and phosphoric acid-doped PBI (PA-PBI) membranes exhibit not only good proton conductivity [2,13–23] and low gas permeability [24–26], but also almost zero electro-osmotic drag [27,28],

* Corresponding author. Tel.: +1 604 221 3087.
E-mail address: jiujun.zhang@nrc.gc.ca (J. Zhang).

as well as excellent oxidative and thermal stability [8,9,29]. Little work has dealt with the mechanical stability of PA-PBI membranes. Their mechanical stability decreases with increasing PA-doping level [19,24] and operating temperature [19,24], and increases with increasing molecular weight of PBI [24]. Therefore, it is necessary to select suitable PA-doping level and operating temperatures for a PBI membrane in order to get practical proton conductivity and mechanical stability.

Work has also focused on the theoretical modeling of PBI membrane-based fuel cells [30–34], fuel cell components and performance degradation [35–38]. The oxygen reduction reaction (ORR) at elevated temperature and low relative humidity (RH) on platinum (Pt) interfaced with PA-PBI has also been studied [39,40]. With respect to performance, the effects of PBI based membrane electrode assembly (MEA) components and fuel cell operation conditions on performance were studied in relative detail [2,20,41–45].

In the effort to develop high-temperature PEMFC testing and diagnosis capabilities, PEMFC hardware design and the corresponding fuel cell performance with PA-PBI-based MEAs have been validated in our laboratory in a wide temperature range, from 23 to 300 °C [46]. In this paper, fuel cell reaction kinetics, in particular ORR kinetics, is systematically investigated in a high-temperature range of 120–200 °C, using the techniques of fuel cell polarization, AC impedance spectroscopy and cyclic voltammetry. The dependence of fuel cell performance on temperature and oxygen stoichiometry is also studied.

2. Experimental

MEAs used in this work were PA-PBI membrane based, purchased from PEMEAS Fuel Cell Technologies. Pt-based catalysts were used in both the anode and the cathode catalyst layers with a total Pt loading of $1.7 \, \text{mg cm}^{-2}$. The active area of the MEAs was $2.6 \, \text{cm}^{-2}$. The MEAs were tested in the temperature range of 120–200 °C using in-house single cell hardware with serpentine flow channels in the flow field plates. A bladder pressure of 5 atm was used to hold the single cell together and provide sufficient electrical contact between the MEA and the graphite bipolar plates. The compressed air and bottled hydrogen (both of which are dry gases at 0% RH) were directly used as oxidant and fuel, respectively. In this work, we used air as the oxidant rather than pure oxygen. This is because from the point of view of commercialization and real applications of PEM fuel cells, usage of air is more practical to operate PEM fuel cells. In our previous experiments, at the same operating conditions, the performance of a fuel cell operated using oxygen is always better than that of one using air due to the increased oxygen partial pressure. The Tafel slopes for both air and pure O_2 are almost the same, suggestion that the mechanism is almost independent on the O_2 concentration. The flow rates of these feed gases were controlled by their respective mass flow controllers (MFCs). The two MFCs can provide air- and hydrogen-flow rates in the range of 0.02–1.00 standard litres per minute (SLPM). In this study, the H_2 stoichiometry (ST_{H_2}) was fixed at 1.5, while the air stoichiometry (ST_{air}) was varied from 2.0 to 10.00. All tests were conducted at ambient backpressure.

A Fideris^{TM} 100 W test station controlled with FC Power software was used for polarization data collection. For cathode (or anode) surface cyclic voltammetric measurements, a Solartron 1287 potentiostat was used with the working electrode probe connected onto the cathode (or anode) and the counter and reference electrode probes connected onto the anode (or cathode). In this case, the anode (or cathode) served as both the reference and counter electrodes. During the measurements, the cathode (or anode) compartment was flushed with pure N_2 gas while the anode (or cathode) compartment was simultaneously flushed with H_2 gas. For the anode (or cathode) catalyst layer electrochemical Pt surface are (EPSA) measurements, the anode (or cathode) side was flushed with N_2 and the cathode (or anode) was simultaneously flushed with H_2, where the cathode (or anode) served as both the reference electrode and the counter electrode. The charges under those two hydrogen surface waves on the voltammogram near 150 and 230 mV (versus SHE), respectively, were used to estimate the EPSA by adopting a well-recognized value of $210 \, \mu\text{C cm}^{-2}$ for hydrogen electrochemical adsorption/desorption on a smooth Pt surface.

For AC impedance spectroscopic measurements, a Solartron FRA 1252 was used in the frequency range of 10,000–0.01 Hz. AC impedance experiments at OCV were also conducted in order to obtain the apparent exchange current densities (AECDs) of the cathodic ORR and the anodic hydrogen oxidation reaction (HOR). For the measurement of AECD of ORR, the anode side and cathode side were flushed with H_2 and air, respectively, while for the measurement of AECD of HOR, both the anode side and the cathode side were flushed with hydrogen.

3. Results and discussion

3.1. Fuel cell performance as a function of temperature

Polarization curves were obtained using PA-PBI-based MEAs at different temperatures and ambient backpressure with dry hydrogen and air as reactant gases, as shown in Fig. 1. It can be seen that fuel cell performance can be significantly improved from 120 to 200 °C. At the current density of $1.0 \, \text{A cm}^{-2}$, the
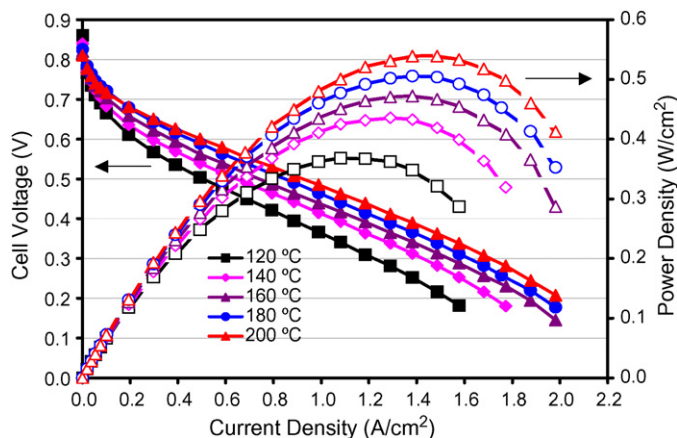

Fig. 1. Polarization curves obtained at ambient back pressure, 0% RH and different temperatures (as marked). $ST_{H_2} = 1.5$, $ST_{air} = 2.0$.

cell voltages are 0.366 V (120 °C), 0.415 V (140 °C), 0.44 V (160 °C), 0.465 V (180 °C) and 0.485 V (200 °C). It is worthwhile to note that the performance at 160 °C is very close to that reported by PEMEAS Fuel Cell Technologies under the same operation conditions [47]. Polarization curves were also recorded at different temperatures with different oxygen stoichiometries such as 4.0, 6.0 and 10.0 (not shown here). For all stoichiometries, the performance has the same trend as that at ST_{air} of 2.0; that is, the higher the temperature, the higher the performance. This observation is consistent with the reported H_2/O_2 [2,43,44] and H_2/air [34,48] performances for PBI-based MEAs.

It can be also observed from Fig. 1 that the gaps between polarization curves for two adjacent temperatures decreases slightly with an increase in temperature. For example, at the current density of 1.0 A cm^{-2}, the voltage difference between 120 and 140 °C is 49 mV, while the voltage differences between 140 and 160 °C, 160 and 180 °C, and 180 and 200 °C are 29, 25 and 20 mV, respectively. This may indicate that the temperature effect on fuel cell performance is more pronounced at lower temperatures than at higher temperatures.

Fig. 2 shows the MEA maximum power densities as a function of temperature. A nearly linear increase of power density with increasing temperature can be observed, indicating the benefit of high-temperature operation. This observation is consistent with our previous work using Nafion-based MEAs in the temperature range of 23–120 °C [49].

In this work, we did not run lifetime tests of the MEA at OCV. This information will be in further work. According to reference [38], the performance of MEA decreased after 244.5 h at OCV tests. EIS indicated that both the cathode activation resistance and the mass transport resistance increased significantly. XRD showed that the cathode Pt crystallite size increased to as much as 5.3 times its original value.

3.2. Temperature effect on exchange current densities of fuel cell reactions

In order to get the AECD (A cm^{-2}) of cathodic ORR and anodic HOR, AC impedance was conducted at fuel cell OCV

conditions from 120 to 200 °C. The method used to obtain the values of these kinetic parameters has been described in our previous papers [49,50], in which the Bulter-Volmer theory was used to simulate fuel cell performance. The Bulter-Volmer theory can be expressed as follows for cathodic and anodic reactions, respectively:

$$I_c = i^o_{O_2} \frac{P_{O_2}}{P^{OCV}_{O_2}} (e^{n_{\alpha O} \alpha_O F\eta_c/RT} - e^{-n_{\alpha O}(1-\alpha_O)F\eta_c/RT}) \tag{1}$$

$$I_a = i^o_{H_2} \frac{P_{H_2}}{P^{OCV}_{H_2}} (e^{n_{\alpha H} \alpha_H F\eta_a/RT} - e^{-n_{\alpha H}(1-\alpha_H)F\eta_a/RT}) \tag{2}$$

In Eqs. (1) and (2), R is the gas constant (8.314 J mol^{-1} K^{-1}), T the temperature (K), F the Faradic constant (96,487 C mol^{-1}), I_c and I_a the cathode and anode current densities, respectively; while $i^o_{O_2}$ and $i^o_{H_2}$ and are the AECDs for ORR and HOR at OCV, respectively. η_c and η_a are the cathodic and anodic overpotentials, respectively. The α_O and α_H are the electron transfer coefficients for ORR and HOR, respectively. $\eta_{\alpha O}$ and $\eta_{\alpha H}$ are the electron transfer numbers in the rate-determining steps for ORR and HOR, respectively. $P^{OCV}_{O_2}$ and P_{O_2} are the partial pressures of O_2 in the cathode chamber at fuel cell OCV and polarization, respectively. $P^{OCV}_{H_2}$ and P_{H_2} are the partial pressures of H_2 in the anode chamber at fuel cell OCV and polarization, respectively. If the values of parameters such as $i^o_{O_2}$, α_O, $\eta_{\alpha O}$, $P^{OCV}_{O_2}$, P_{O_2}, $i^o_{H_2}$, α_H, $\eta_{\alpha H}$, $P^{OCV}_{H_2}$ and P_{H_2}, are known, the η_c and η_a can be deduced at each current density. Then, by putting η_c and η_a into Eq. (3), V_{cell} can be simulated if E^{OCV} and the membrane resistance (R_m) are known. In Eq. (3), V_{cell} is the fuel cell voltage at current density of I_{cell}.

$$V_{cell} = E^{OCV} - \eta_c - \eta_a - I_{cell}R_m \tag{3}$$

Fig. 3 compares the simulated and measured fuel cell performances at different temperatures for current densities less than 0.4 A cm^{-2}. The simulated and measured data for each curve are fairly consistent, confirming that the measured exchange current densities are reliable.

Note that the AECDs for ORR at fuel cell OCVs measured by the AC impedance method may contain contributions from the oxidation reaction of H_2 that has crossed over from the
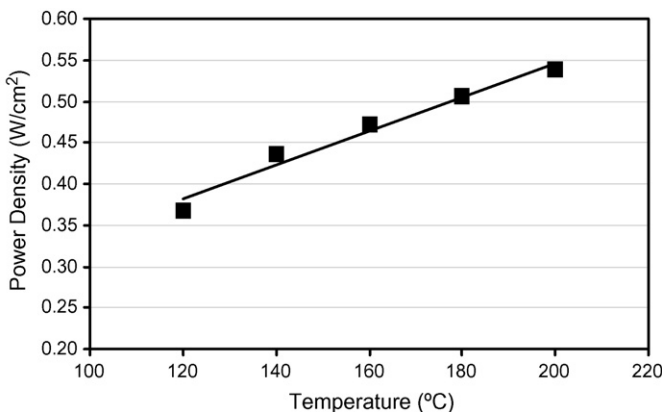

Fig. 2. Maximum power density of the PA-PBI-based membrane electrode assembly (MEA) as a function of temperature. Data from Fig. 1.
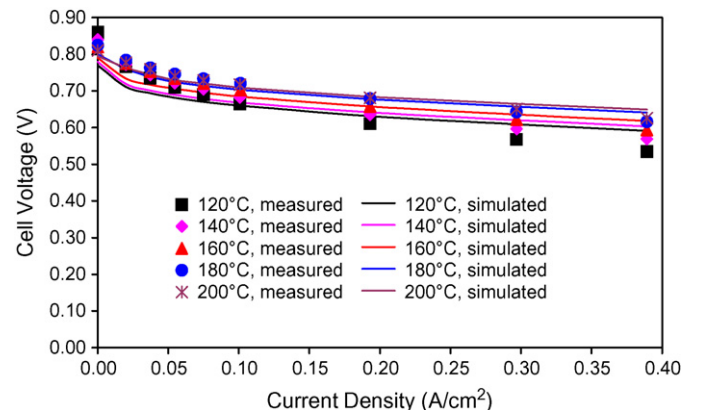

Fig. 3. Measured and simulated polarization curves as a function of current density at different temperatures.

Table 1
Apparent and intrinsic exchange current densities at different temperatures in the low current density range, measured at ambient pressure and 0% RH

	Temperature (°C)				
	120	140	160	180	200
$i^o_{O_2}$, apparent (A cm^{-2})	2.30×10^{-3}	2.05×10^{-3}	2.64×10^{-3}	3.60×10^{-3}	5.43×10^{-3}
$I^o_{O_2(Pt/PtO)}$, intrinsic (A cm^{-2})	8.97×10^{-5}	1.05×10^{-4}	1.51×10^{-4}	3.18×10^{-4}	7.88×10^{-4}
$i^o_{H_2}$, apparent (A cm^{-2})	0.72	1.24	1.88	2.50	2.71
$I^o_{H_2(Pt)}$, intrinsic (A cm^{-2})	1.02×10^{-2}	2.18×10^{-2}	3.51×10^{-2}	6.82×10^{-2}	1.16×10^{-1}

anode, and contributions from the PtO/Pt redox reaction [50,51]. However, since the two reactions are faster than ORR, their contributions to the exchange current density measurements could be negligible. Based on measured ORR AECDs ($i^o_{O_2}$) and HOR AECDs ($i^o_{H_2}$), the intrinsic exchange current densities (IECDs) for ORR and HOR can be calculated according to Eqs. (4) and (5),

$$i^o_{O_2} = (EPSA)_c \, I^o_{O_2(Pt/PtO)} \left(\frac{P_{O_2}}{P^o_{O_2}} \right)^{0.001678T} \qquad (4)$$

$$i^o_{H_2} = (EPSA)_a \, I^o_{H_2(Pt)} \left(\frac{P_{H_2}}{P^o_{H_2}} \right)^{0.5} \qquad (5)$$

where $(EPSA)_c$ and $(EPSA)_a$ are the electrochemical Pt surface areas of the cathode and anode catalyst layers, respectively, with a unit of cm^2 Pt surface per cm^2 electrode geometric area (cm^2 cm^{-2}); $I^o_{O_2(Pt/PtO)}$ and $I^o_{H_2(Pt)}$ are the IECDs of O$_2$ reduction on a Pt/PtO surface and of H$_2$ oxidation on a Pt surface, respectively; and $P^o_{O_2}$ and $P^o_{H_2}$ are the standard pressures of O$_2$ and H$_2$, respectively. The obtained parameter values at different temperatures are listed together in Table 1.

Table 1 shows that temperature has a significant effect on the IECDs for both ORR and HOR; that is, the higher the temperature, the larger the exchange current densities. This trend is consistent with our previous results for a Nafion-based PEM fuel cell in the temperature range of 23–120 °C [49]. Table 1 also shows that the IECD of HOR is much higher ($\sim 10^{-3}$ times) than that of ORR. This indicates that the fuel cell reaction kinetics is determined by the ORR.

The relationship between activation energy and the IECD should follow the Arrehnius theory [49]:

$$\ln(I^o_{O_2(Pt/PtO)}) = \ln(I^{ut}_{O_2(Pt/PtO)}) - \frac{E^{O_2}_a}{R} \left(\frac{1}{T} \right) \qquad (6)$$

$$\ln(I^o_{H_2(Pt)}) = \ln(I^{ut}_{H_2(Pt)}) - \frac{E^{H_2}_a}{R} \left(\frac{1}{T} \right) \qquad (7)$$

where $I^{ut}_{O_2(Pt/PtO)}$ and $I^{ut}_{H_2(Pt)}$ are the ORR and HOR IECDs at unlimited temperature value, respectively. $E^{O_2}_a$ and $E^{H_2}_a$ are the activation energies for ORR and HOR, respectively.

Fig. 4 shows the logarithm IECDs as a function of the reciprocal of temperature. The activation energies can be obtained from the slopes of the two plots. Activation energies of 46.2 kJ mol^{-1} for anode HOR and 41.4 kJ mol^{-1} for cathode ORR are obtained.
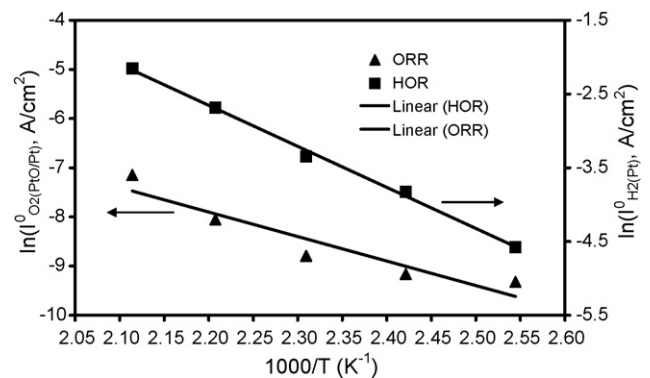

Fig. 4. The IECDs of cathodic ORR and anodic HOR as a function of the reciprocal of temperature in the fuel cell current density range of <0.4 A cm^{-2} (kinetic range). Data from Table 1.

3.3. AC impedance diagnosis for fuel cell performance

In order to get a better understanding of the effect of temperature on fuel cell performance, AC impedance spectroscopy was used to diagnose the fuel cell. Fig. 5 shows the in situ AC impedance spectrum of a PEM fuel cell operated at 140 °C and ambient pressure with a current density of 0.2 A cm^{-2}. There are two semicircles on the spectrum, one in the high-frequency domain and the other in the low-frequency domain. Similar spectra have been widely reported in the literature for PEM fuel cells [52,53]. The intercept in the high-frequency domain on the Re axis of Fig. 5 represents the ohmic resistance of the
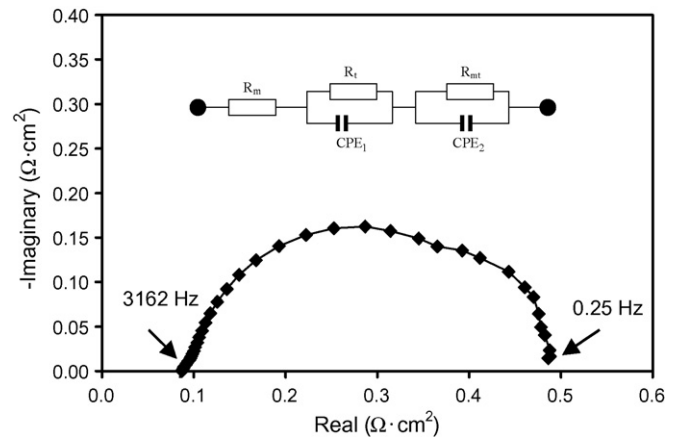

Fig. 5. Nyquist plot for a fuel cell operated at 140 °C and ambient pressure with a current density of 0.2 A cm^{-2}. Insert is the proposed equivalent circuit mode for PEM fuel cell. ST$_{H_2}$ = 1.5, ST$_{air}$ = 2.0.

fuel cell, which is dominated by membrane resistance. Thus, the membrane resistance in real fuel cell operating conditions can be measured. The first semicircle represents the fuel cell reaction kinetics, contributed to by both the cathodic ORR and anodic HOR processes. The second semicircle represents the mass transfer process, contributed to by the diffusion of oxygen and hydrogen to the Pt active surfaces and the proton transfer resistance within the catalyst layers. The insert in Fig. 5 shows a proposed equivalent circuit used to simulate the impedance data in this paper. R_m is the high-frequency resistance (the intercept on the Re axis at the high-frequency end), which represents the membrane resistance. R_t is the charge transfer resistance, and CPE$_1$ (constant phase element) represents the R_t-associated catalyst layer capacitance properties. R_{mt} is the resistance related to the mass transfer processes of gas (O$_2$ and H$_2$) diffusions in the catalyst layers. CPE$_2$ represents the R_{mt}-associated capacitance.

3.3.1. Temperature effect on membrane resistance

For example, Fig. 6 shows the membrane resistance as a function of current density at two typical temperatures (160 and 200 °C). The membrane resistances here represent the proton transfer resistances within the fuel cell membrane, which were measured by AC impedance spectroscopy. The values are in the range of 0.08–0.11 Ω cm^{-2}, close to that for a Nafion membrane under fully humidified conditions at 80 °C, and consistent with the result reported by Jalani et al. [48]. The membrane resistance in the studied current density range decreases as temperature increases from 120 to 200 °C. This is consistent with results reported by Ma et al. [16] and He et al. [17] for the resistances of PBI-based membranes.

The proton conductivity mechanism of the PBI-based membrane is different from that of a PFSA-based membrane. The widely accepted mechanism for PBI is proton hopping (the protons transfer from one carrier to another via hydrogen bonds) [15,54]. During the proton transfer, there is no net transport of any carrier species across the membrane. For a Nafion-based

membrane, proton migration occurs via the vehicle mechanism; the protons diffuse through the medium via the solvated hydrogen ion species, H$_3$O$^+$. For a vehicle mechanism, conductivity follows Eq. (8) [55–57],

$$\sigma = A \exp\left(-\frac{E_a}{RT}\right) \tag{8}$$

while, for a hopping mechanism, conductivity follows Eq. (9) [15–17,19,54],

$$\sigma = \frac{A}{T} \exp\left(-\frac{E_a}{RT}\right) \tag{9}$$

According to Eq. (9), the membrane conductivity of PBI, a reciprocal of the membrane resistance measured in this work, can be quantitatively described by Eq. (10) [15–17,19,54],

$$\ln(\sigma T) = \ln(\sigma_0) - \frac{E_a^m}{R}\left(\frac{1}{T}\right) \tag{10}$$

where σ, σ_0, E_a^m, R and T are the membrane conductivity (S cm^{-1}), the pre-exponential factor (S K^{-1} cm^{-1}), the proton conducting activation energy (kJ mol^{-1}), the ideal gas constant (J mol^{-1} K^{-1}) and the temperature (K), respectively. According to Eq. (10), the plot of $\ln(\sigma T)$ versus $1/T$ allows one to obtain the values of E_a^m and $\ln(\sigma_0)$. Table 2 shows the obtained values of E_a^m and $\ln(\sigma_0)$ at several typical current densities. It can be seen that both parameters are almost independent of the current densities, indicating that fuel cell operating load has no effect on the proton conducting mechanism of the studied PA-PBI membranes. The average values for these two parameters are 19.9 kJ mol^{-1} and 10.8 S K^{-1} cm^{-1}, respectively, close to the reported values of ~28 kJ mol^{-1} and ~10 S K^{-1} cm^{-1} at the phosphoric acid-doping level of 630% and the RH of 5% [16].

Fig. 6 also shows that the membrane resistance can change with increasing current density. In the low current density region (<1.0 A cm^{-2}), membrane resistance decreases with increasing current density. This could be because more and more water was produced by the electrochemical reaction at the cathode when the current density was increased, resulting in an increase in the proton conductivity of the PBI membrane [16,17]. In the
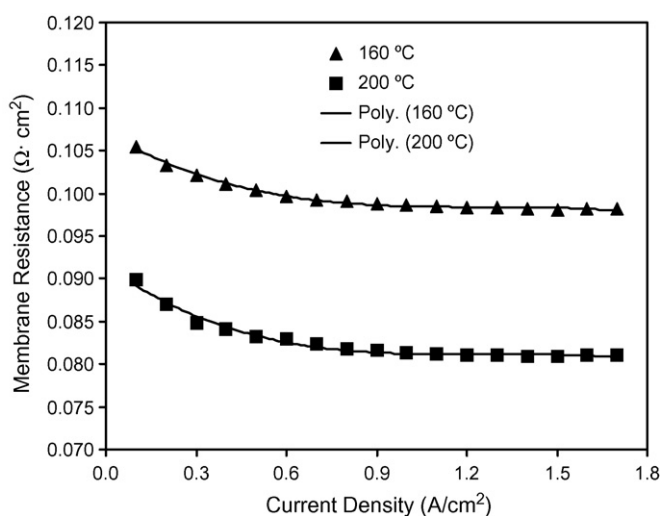

Fig. 6. Membrane resistance as a function of current density. Data were obtained from in situ AC impedance of PA-PBI-based fuel cells operated at different temperatures and ambient pressure. ST$_{H_2}$ = 1.5, ST$_{air}$ = 2.0.

Table 2
Proton conducting activation energies and pre-exponential factors for a PA-PBI-based MEA at different fuel cell current densities in the temperature range of 120–200 °C, with ambient backpressure and 0% RH

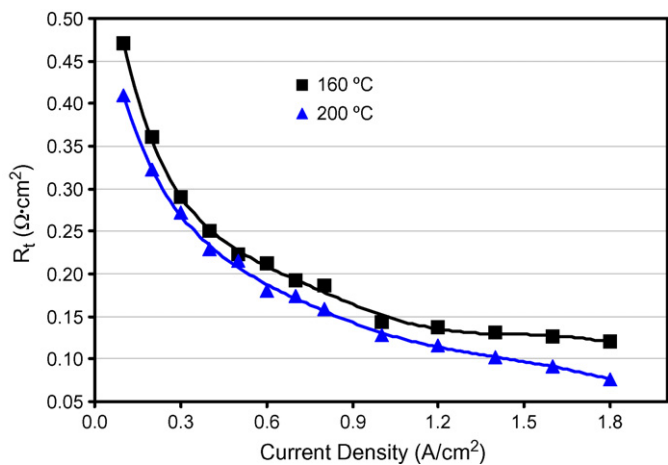| Current density (A cm^{-2})	Proton conducting activation energies (E_a^m) (kJ mol^{-1})	Pre-exponential factor ($\ln(\sigma_0)$) (S K^{-1} cm^{-1})
0.1	18.9	10.5
0.3	19.7	10.7
0.5	19.9	10.8
0.8	20.1	10.8
1.0	20.1	10.8
1.2	20.1	10.9
1.4	20.0	10.8
1.6	20.2	10.9
Average	19.9	10.8

ST$_{H_2}$ = 1.5, ST$_{air}$ = 2.0.

Fig. 7. Charge transfer resistances as a function of current density at two different temperatures. $ST_{H_2} = 1.5$, $ST_{air} = 2.0$.

Fig. 8. Gas transfer resistances as a function of current density at two different temperatures (in high current density region). $ST_{H_2} = 1.5$, $ST_{air} = 2.0$.

high current density region ($>1.0\,A\,cm^{-2}$), a balance between the produced water and the purged water can be established, resulting in a constant water-content level within the membrane, which is reflected by a constant resistance level.

3.3.2. Temperature effect on charger transfer resistance

Fig. 7 shows the fuel cell charge transfer resistances measured by in situ AC impedance spectroscopy at two typical temperatures. It can be seen that the charge transfer resistances decrease with increasing temperature, suggesting that the increasing temperature can effectively speed up the fuel cell reaction kinetics. In fact, both cathode ORR and anode HOR should contribute to the measured R_t. In the low current density range, the anode polarization contribution may be negligible compared to that of the cathode. The R_t could be considered to be the charger transfer resistance of ORR. However, in the high current density range, the anode polarization contribution may need to be considered [49]; thus, the R_t cannot be considered as the ORR charger transfer resistance here [49].

3.3.3. Temperature effect on mass transfer resistance

Mass transfer in fuel cell catalyst layers includes two primary parts: the diffusion of oxygen to the cathode Pt active surface and the diffusion of hydrogen to the anode Pt active surface in the catalyst layers. Temperature can significantly affect the mass transfer in a fuel cell catalyst layer. At current densities higher than $0.4\,A\,cm^{-2}$, the dominant process will be the gas transfer. Jalani et al. [48] found that the mass transfer losses due to gas diffusion are profound at current densities greater than $0.4\,A\,cm^{-2}$. In our previous study, similar behaviour was also observed [58].

For example, Fig. 8 shows the gas transfer resistances measured at different temperatures in the current density range of greater than $1.0\,A\,cm^{-2}$. It can be seen that the gas transfer resistance increases with increasing temperature. This trend is opposite to those of proton transfers in the membrane/catalyst layers and ORR/HOR reaction charger transfer, shown in Figs. 6 and 7. This could be interpreted as a trade-off of the temperature dependent gas diffusivity and solubility in the cat-
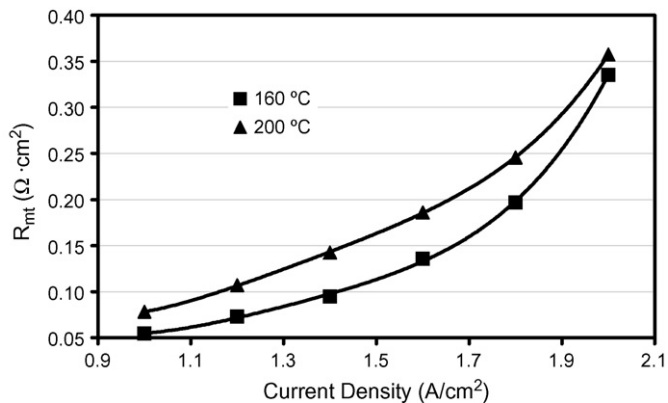
alyst layers. Increasing temperature can effectively increase the gas diffusivity but reduce the solubility (or gas concentration in the diffusion medium). The increased diffusivity will result in a reduced gas diffusion resistance. However, the reduced gas solubility will result in an increase in gas diffusion resistance. For the case shown in Fig. 8, the effect of the reduced gas solubility might be larger than the effect of the increased gas diffusivity, yielding an increased gas diffusion resistance when the temperature is increased.

3.4. Stoichiometry effect on fuel cell performance

Fig. 9 shows the polarization curves obtained at $160\,^\circ C$ with different oxygen stoichiometries (ST_{air}). The fuel cell performance increases as ST_{air} increases from 2.0 to 10.0. This performance improvement is pronounced in the high current density region. On the other hand, the maximum power density can also be increased considerably. For example, at a cell voltage of 0.3 V, the current density is increased from 1.57 to $2.07\,A\,cm^{-2}$ from stoichiometries of 2.0–10.0, resulting in an increase of maximum power density from 0.472 to $0.624\,W\,cm^{-2}$. In order to understand the effect of the oxygen stoichiometry on performance, the AC impedance spectroscopic
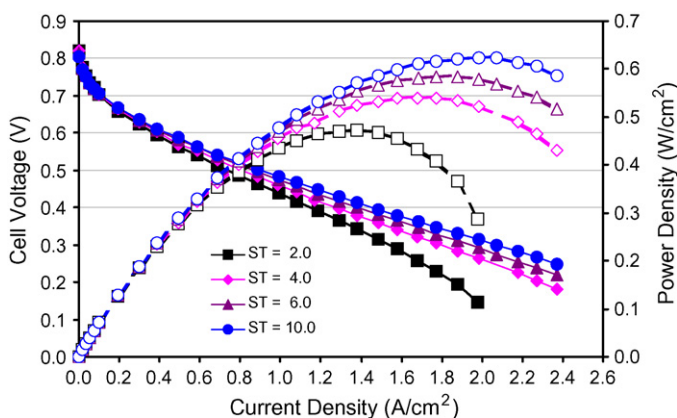

Fig. 9. Polarization curves obtained at $160\,^\circ C$, ambient pressure and 0% RH with different oxygen stoichiometries (as marked). $ST_{H_2} = 1.5$.
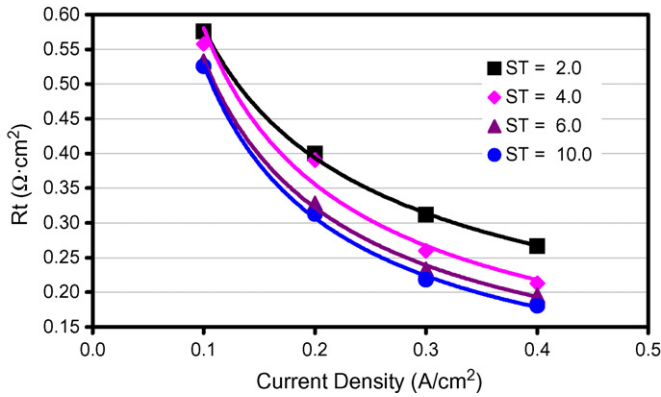
Fig. 10. Charge transfer resistances as a function of current density with different oxygen stoichiometries (as marked) in the low current density region. $ST_{H_2} = 1.5$. Cell temperature: 120 °C.

technique was used for diagnosis, as described in the following sections.

3.4.1. Effect of oxygen stoichiometry on membrane resistance

It was observed that there was no significant effect of the oxygen stoichiometry on the membrane resistance. For example, when ST_{air} was increased from 2.0 to 10.0, a membrane resistance increase of only approximately 3% could be observed in the current density range of 0–2.0 A cm^{-2} at the studied temperatures (120, 140, 160, 180 and 200 °C).

3.4.2. Effect of oxygen stoichiometry on fuel cell reaction thermodynamics and kinetics

Fig. 10 shows an example of the change in charger transfer resistance with oxygen stoichiometry at 120 °C. A significant kinetic improvement can be seen when the ST_{air} is increased. This improvement can be largely attributed to the oxygen partial pressure increase exerted by the increased air flow rate. Fig. 11 shows the average O_2 partial pressure inside the cathode as a function of ST_{air} at 140 °C; the increase in O_2 partial pressure with increasing ST_{air} can be seen clearly. The oxygen partial pressures (P_{O_2}) in Fig. 11 are the averaged values over the partial
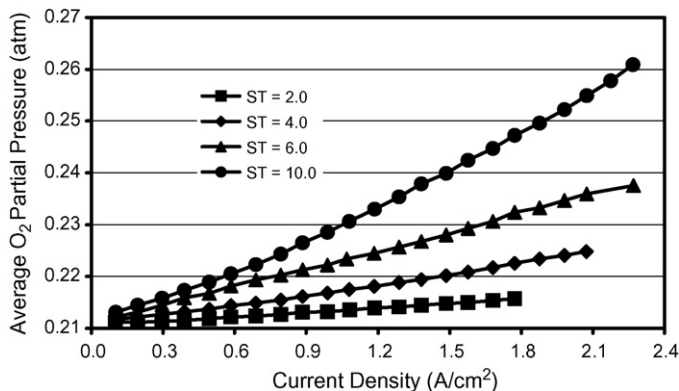
pressure values at the fuel cell inlet and outlet, assuming that the partial pressure distribution along the flow field channel is linear. From kinetic Eq. (1), it can be seen that an increase in O_2 partial pressure can effectively enhance the fuel cell reaction kinetics due to the fact that the fuel cell current density is proportional to the P_{O_2}.

Thermodynamically, the Nernst equation can be used to describe the effect of gas partial pressures on the O_2/H_2 fuel cell OCV:

$$E^{OCV} = E^{\circ} + \frac{RT}{2F} \ln \left(\frac{P_{H_2} P_{O_2}^{1/2}}{P_{H_2O}} \right) \tag{11}$$

where E° is the ideal standard potential for fuel cell reaction, and P_{H_2O} is the partial pressure of the water vapour. According to Eq. (11), an increase in the partial pressure of a reactant such as O_2 can increase fuel cell OCV, resulting in an improvement in fuel cell thermodynamics. On the other hand, according to Eq. (3), with an increase in E^{OCV}, the fuel cell performance throughout the whole current density range will be improved.

3.4.3. Effect of O_2 stoichiometry on the mass transfer process

Similar to the effect of temperature, the effect of ST_{air} on the mass transfer process in the low current density region was different from that in high current density region. In the low current density region (<0.4 A cm^{-2}), the effect on the performance was not pronounced, suggesting that O_2 stoichiometry has a negligible effect on the proton transfer process inside the catalyst layer.

In the high current density range (>1.0 A cm^{-2}), a significant effect of ST_{air} on the gas transfer process was observed. Fig. 12 shows the Nyquist plots measured at the current density of 1.5 A cm^{-2} with different O_2 stoichiometries. The second semicircle in the low frequency region represents the mass transfer resistance in the catalyst layer, which is shrunk with increasing ST_{air}. This means that the gas transfer resistance in the catalyst layer is decreased when ST_{air} is increased. The simulated gas transfer resistances as a function of current density
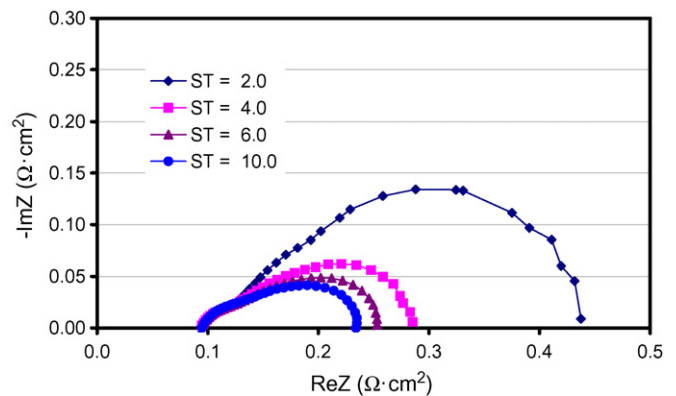

Fig. 11. Average O_2 partial pressures as a function of current density at 140 °C, ambient pressure and 0% RH with different O_2 stoichiometries. $ST_{H_2} = 1.5$.

Fig. 12. Nyquist plots measured at the current density of 1.5 A cm^{-2}, 120 °C, ambient pressure and 0% RH with different O_2 stoichiometries (as marked). $ST_{H_2} = 1.5$.
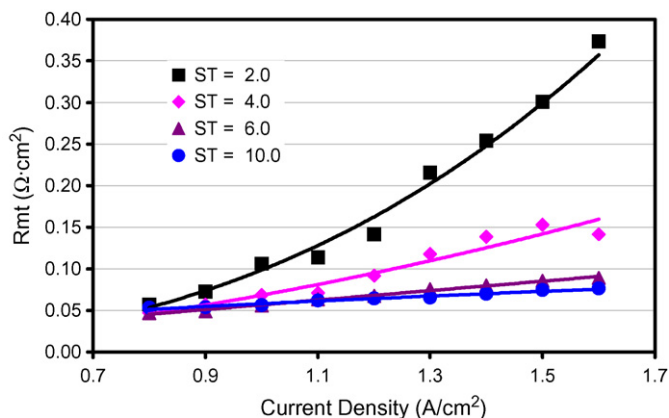
Fig. 13. Gas transfer resistances at 120 °C, ambient pressure and 0% RH with different O_2 stoichiometries. $ST_{H_2} = 1.5$.

at different ST_{air} are shown in Fig. 13. Therefore, increasing O_2 stoichiometry will benefit fuel cell performance by speeding up the gas transfer process inside the catalyst layers.

4. Conclusions

PA-PBI membrane-based PEM fuel cells were tested in the temperature range of 120–200 °C, with ambient pressure and 0% RH. The exchange current densities for cathodic ORR and anodic HOR on Pt-based catalysts at such high temperatures were obtained through AC impedance spectroscopy, surface cyclic voltammetry and fuel cell performance simulation. The activation energies for ORR, HOR and membrane proton conductivity were also obtained separately. The activation energy of membrane proton conductivity is almost independent of the current densities, indicating that the fuel cell operating load has no effect on the proton conducting mechanism of the studied PA-PBI membranes.

Temperature showed significant effects on the charger transfer and proton transfer resistances; that is, the resistances were reduced when the temperature was increased, suggesting that increasing temperature can effectively speed up these kinetic processes inside a fuel cell. However, an opposite effect of temperature on the gas (O_2 and H_2) diffusion processes inside the catalyst layers was observed, indicating that increasing temperature can slow down the gas diffusion processes. This observation could be interpreted by the trade-off of the temperature dependent gas diffusivity and solubility in the catalyst layers.

The effect of ST_{air} on the fuel cell performance was also investigated. Increasing ST_{air} can effectively increase the O_2 partial pressure in the feed air, leading to improvements in both the thermodynamics and the kinetics of the fuel cell reactions. In addition, it was also observed that increasing ST_{air} can improve the gas diffusion processes.

Acknowledgements

References

[1] J. Zhang, Z. Xie, J. Zhang, Y. Tang, C. Song, T. Navessin, Z. Shi, D. Song, H. Wang, D.P. Wilkinson, J. Power Sources 160 (2006) 872.
[2] Q. Li, R. He, J.-A. Gao, J.O. Jensen, N.J. Bjerrum, J. Electrochem. Soc. 150 (2003) A1599–A1605.
[3] T. Kyu, M. Hashiyama, A. Eisenberg, Can. J. Chem. 61 (1983) 680.
[4] K.Y. Cho, H.Y. Jung, N.S. Choi, S.J. Sung, J.K. Park, J.H. Choi, Y.E. Sung, Solid State Ionics 176 (2005) 3027.
[5] K.T. Adjemian, S.J. Lee, S. Srinivasan, J. Benziger, A.B. Bocarsly, J. Electrochem. Soc. 149 (2002) A256–A261.
[6] P. Costamagna, C. Yang, A.B. Bocarsly, S. Srinivasan, Electrochim. Acta 47 (2002) 1023.
[7] A. Collier, H. Wang, X. Zi Yuan, J. Zhang, D.P. Wilkinson, Int. J. Hydrogen Energy 31 (2006) 1838.
[8] P. Musto, F.E. Karasz, W.J. MacKnight, Polymer 34 (1993) 2934.
[9] S.R. Samms, S. Wasmus, R.F. Savinell, J. Electrochem. Soc. 143 (1996) 1225.
[10] B. Xing, O. Savadogo, J. New Mater. Electrochem. Syst. 2 (1999) 95.
[11] M.F.H. Schuster, W.H. Meyer, M. Schuster, K.D. Kreuer, Chem. Mater. 16 (2004) 329.
[12] T. Dippel, K.D. Kreuer, J.C. Lassegues, D. Rodriguez, Solid State Ionics 61 (1993) 41.
[13] J.S. Wainright, J.T. Wang, D. Weng, R.F. Savinell, M. Litt, J. Electrochem. Soc. 142 (1995) L121–L123.
[14] S.L.-C.H. Shih-Wei Chuang, J. Polym. Sci., Part A: Polym. Chem. 44 (2006) 4508.
[15] R. Bouchet, E. Siebert, Solid State Ionics 118 (1999) 287.
[16] Y.-L. Ma, J.S. Wainright, M.H. Litt, R.F. Savinell, J. Electrochem. Soc. 151 (2004) A8–A16.
[17] R. He, Q. Li, G. Xiao, N.J. Bjerrum, J. Membrane Sci. 226 (2003) 169.
[18] J. Lobato, P. Canizares, M.A. Rodrigo, J.J. Linares, G. Manjavacas, J. Membrane Sci. 280 (2006) 351.
[19] L. Qingfeng, H.A. Hjuler, N.J. Bjerrum, J. Appl. Electrochem. 31 (2001) 773.
[20] Q. Li, R. He, J.O. Jensen, N.J. Bjerrum, Fuel Cells 4 (2004) 147.
[21] J.J. Fontanella, M.C. Wintersgill, J.S. Wainright, R.F. Savinell, M. Litt, Electrochim. Acta 43 (1998) 1289.
[22] L. Xiao, H. Zhang, E. Scanlon, L.S. Ramanathan, E. Choe, D. Rogers, T. Apple, B.C. Benicewicz, Chem. Mater. 17 (2005) 5328.
[23] M. Kawahara, J. Morita, M. Rikukawa, K. Sanui, N. Ogata, Electrochim. Acta 45 (2000) 1395.
[24] R. He, Q. Li, A. Bach, J.O. Jensen, N.J. Bjerrum, J. Membrane Sci. 277 (2006) 38.
[25] H.-J. Kim, T.-H. Lim, J. Ind. Eng. Chem. 10 (2004) 1081.
[26] A.M. Fisher, S.R. Samms, J. Hallmark, R. Koripella, S. Roger, B. Mylan, Prep. Sym. Am. Chem. Soc., Div. Fuel Chem. 49 (2004) 792.
[27] D. Weng, J.S. Wainright, U. Landau, R.F. Savinell, J. Electrochem. Soc. 143 (1996) 1260.
[28] X. Ren, W. Henderson, S. Gottesfeld, J. Electrochem. Soc. 144 (1997) L267–L270.
[29] J.A. Asensio, S. Borros, P. Gomez-Romero, J. Polym. Sci.: Part A: Polym. Chem. 40 (2002) 3703.
[30] D. Cheddie, N. Munroe, Int. J. Transport Phenom. 8 (2006) 51.
[31] D. Cheddie, N. Munroe, J. Power Sources 156 (2006) 414.
[32] D. Cheddie, N. Munroe, Energy Convers. Manage. 47 (2006) 1490.
[33] D. Cheddie, N. Munroe, J. Power Sources 160 (2006) 215.
[34] A.R. Korsgaard, R. Refshauge, M.P. Nielsen, M. Bang, S.K. Kaer, J. Power Sources 162 (2006) 239.
[35] Y. Zhai, H. Zhang, D. Xing, Z.G. Shao, J. Power Sources 164 (2007) 126.
[36] Y. Zhai, H. Zhang, G. Liu, J. Hu, B. Yi, J. Electrochem. Soc. 154 (2007) B72–B76.

[37] G. Liu, H. Zhang, J. Hu, Y. Zhai, D. Xu, Z.G. Shao, J. Power Sources 162 (2006) 547.

[38] Z. Qi, S. Buelte, J. Power Sources 161 (2006) 1126.

[39] Z. Liu, J.S. Wainright, M.H. Litt, R.F. Savinell, Electrochim. Acta 51 (2005) 3914.

[40] Z. Liu, J.S. Wainright, R.F. Savinell, Chem. Eng. Sci. 59 (2004) 4833.

[41] F. Seland, T. Berning, B. Borresen, R. Tunold, J. Power Sources 160 (2006) 27.

[42] J. Lobato, P. Canizares, M.A. Rodrigo, J.J. Linares, Electrochim. Acta 52 (2007) 3910.

[43] P. Krishnan, J.S. Park, C.S. Kim, J. Power Sources 159 (2006) 817.

[44] O. Savadogo, B. Xing, J. New Mater. Electrochem. Syst. 3 (2000) 343.

[45] J.-T. Wang, R.F. Savinell, J. Wainright, M. Litt, H. Yu, Electrochim. Acta 41 (1996) 193.

[46] Y. Tang, J. Zhang, C. Song, J. Zhang, Electrochem. Solid-State Lett. 10 (2007) B142.

[47] http://www.pemeas.com/celtecp.asp.

[48] N.H. Jalani, M. Ramani, K. Ohlsson, S. Buelte, G. Pacifico, R. Pollard, R. Staudt, R. Datta, J. Power Sources 160 (2006) 1096.

[49] C. Song, Y. Tang, J.L. Zhang, J. Zhang, H. Wang, J. Shen, S. McDermid, J. Li, P. Kozak, Electrochim. Acta 52 (2007) 2552.

[50] J. Zhang, Y. Tang, C. Song, J. Zhang, H. Wang, J. Power Sources 163 (2006) 532.

[51] X. Cheng, J. Zhang, Y. Tang, C. Song, J. Shen, D. Song, J. Zhang, J. Power Sources 167 (2007) 25.

[52] T.E. Springer, T.A. Zawodzinski, M.S. Wilson, S. Gottesfeld, J. Electrochem. Soc. 143 (1996) 587.

[53] V.A. Paganin, C.L.F. Oliveira, E.A. Ticianelli, T.E. Springer, E.R. Gonzalez, Electrochim. Acta 43 (1998) 3761.

[54] R. Bouchet, S. Miller, M. Duclot, J.L. Souquet, Solid State Ionics 145 (2001) 69.

[55] P.C. Rieke, N.E. Vanderborgh, J. Membrane Sci. 32 (1987) 313.

[56] G. Ye, N. Janzen, G.R. Goward, Macromolecules 39 (2006) 3283.

[57] P. Commer, A.G. Cherstvy, E. Spohr, A.A. Kornyshev, Fuel Cells 2 (2002) 127.

[58] Y. Tang, J. Zhang, C. Song, H. Liu, J. Zhang, H. Wang, S. Mackinnon, T. Peckham, J. Li, S. McDermid, P. Kozak, J. Electrochem. Soc. 153 (2006) A2036–A2043.